INSTITUTE FOR FUSION STUDIES

DOE/ET-53088-492 IFSR #492

Hamiltonian Chaos and Transport in Quasigeostrophic Flows

DIEGO DEL CASTILLO and P.J. MORRISON
Institute for Fusion Studies
The University of Texas at Austin
Austin, Texas 78712

April 1991

E-mail: diego@chaos.utexas.edu
morrison@hagar.ph.utexas.edu

THE UNIVERSITY OF TEXAS

AUSTIN

Hamiltonian Chaos and Transport in Quasigeostrophic Flows

Diego del-Castillo-Negrete and P.J. Morrison
Department of Physics and Institute for Fusion Studies
The University of Texas at Austin
Austin, Texas 78712

April 12, 1991

Abstract

Chaotic advective transport in quasigeostrophic flows is studied. Of particular interest is to compare theory with recent rotating tank experiments [Nature **337**, 58 (1989); *Nonlinear Topics in Ocean Physics*, ed. A. Osborne (North Holland, Amsterdam, 1991)]. Ideas regarding chaotic advection are briefly reviewed. A derivation of the quasigeostrophic equation relevant to the tank experiments is given, from which a model for the stream function is extracted and compared to experimental data. Linear theory is shown to predict correctly the onset of observed sinuous Rossby waves. A model stream function, composed of a zonal flow equilibrium with linear eigenfunctions, is used to study chaotic transport. Upon applying the Chirikov overlap criterion to the model it is seen, in agreement with experiments, that *banded chaos*, i.e., regions of chaos bounded by invariant surfaces (in particular those of the zonal flow barrier), is to be expected. It is also shown that *global chaos*, and hence transport across the zonal flow, is inconsistent with linear theory and in general requires resonances with phase

To appear in American Institute of Physics Proceedings of Feb. 18-20, 1991 meeting in La Jolla, CA, La Jolla International School of Physics, The Institute for Advanced Physics Studies. Research Trends in Physics, *Chaotic Dynamics and Transport in Fluids and Plasmas* (Eds. V. Stephan *et al.*)

velocities near the peak velocity of the zonal flow equilibrium. Speculations regarding the consistency of chaos and conservation of potential vorticity are made.

1. Introduction

In the last few years several authors have successfully applied the methods and ideas of few degree-of-freedom Hamiltonian dynamics to some fluid mechanics problems. In particular passive advection in the velocity field of point vortices and in the Stokes flow that describes journal bearings and cavity flows has been considered. See for example Aref (1984) and the review article by Ottino (1990) for further references. Also, similar ideas have been used in plasma physics to study the $\mathbf{E} \times \mathbf{B}$ motion of charged particles in drift waves (Horton 1985, 1990). Here we consider the modelling of the velocity field and passive advection in rotating fluid flows in the quasigeostrophic regime.

This connection between fluid mechanics and Hamiltonian dynamics is clearly understood if one considers the Lagrangian approach rather than the usual Eulerian approach. According to the latter, the fluid is described by the velocity field $\mathbf{V}(x,y,z,t) = (u,v,w)$ at any point (x,y,z) at all times t. On the other hand, the Lagrangian approach is described by tracking the motion of the fluid particles, which is determined by $\mathbf{X}(\mathbf{a},t)$, the position at time t of a fluid particle that was located at $\mathbf{a}$ at some initial time t_0. The relationship between these two approaches is given by

$$\left(\frac{\partial \mathbf{X}}{\partial t}\right)_{\mathbf{a}} = \mathbf{V}\left(\mathbf{X}(\mathbf{a},t),t\right) \ .$$

Advection is the motion of a scalar field that is transported by the velocity field of the fluid. The scalar field is passive if its presence does not induce changes in the flow field. Two examples of advection of passive scalar fields in fluid visualization experiments are the injection of dye (neglecting molecular diffusion) and the introduction of small neutrally buoyant tracer particles.

In the Lagrangian approach the advection is determined by the following set of ordinary differential equations:

$$\frac{dx}{dt} = u(x,y,t) \qquad \frac{dy}{dt} = v(x,y,t) \qquad \frac{dz}{dt} = w(x,y,t) \tag{1.1}$$

where $(x(t), y(t), z(t))$ represents the trajectory of a fluid particle. The scalar field is assumed to be constant along such a trajectory. If the fluid is two dimensional and incompressible, then the velocity field can be written in terms of a stream function,

$$u = -\frac{\partial \psi}{\partial y} \qquad v = \frac{\partial \psi}{\partial x} \ .$$

In this case Eqs. (1.1) become

$$\frac{dx}{dt} = -\frac{\partial \psi}{\partial y} \qquad \frac{dy}{dt} = \frac{\partial \psi}{\partial x} \ . \tag{1.2}$$

Thus the motion of fluid particles, and hence the motion of a passive scalar quantity in two-dimensional incompressible flow is mathematically analogous to a one degree-of-freedom, possibly time-dependent, Hamiltonian dynamics problem, with the stream function playing the role of the Hamiltonian and the spatial (x, y) coordinates playing the role of canonically conjugate variables. In the study of particle motion in plasmas, the Hamiltonian is the electrostatic potential of the low frequency drift waves. The fact that time-dependent, one degree-of-freedom Hamiltonians generally have chaotic trajectories results in the phenomenon that has been called chaotic advection [Aref (1984)], or Lagrangian turbulence. In this analogy barriers to transport in the fluid and plasma systems are identified with invariant tori of the corresponding Hamiltonian model whereas, regions of mixing or stochastic transport in the fluid and plasma system correspond to chaotic regions in the Hamiltonian model.

The purpose of the present work is to study some of the chaotic advection, transport and mixing properties of a rotating fluid in the quasigeostrophic regime (Pedlosky 1987), using this analogy between fluid systems and Hamiltonian mechanics. In particular we are interested in providing a theoretical framework for understanding the recent experimental results of Sommeria, Meyers and Swinney (hereafter SMS) (1989, 1991), concerning the propagation of Rossby waves in eastward jets. We anticipate that the modelling of this

well-controlled experiment will shed some light on the processes occurring in real planetary atmospheres.

The present work extends and complements two recent works, R.P. Behringer *et al.* (1991) and L.M. Polvani and J. Touma (1991), which proposed models for describing the SMS experiments. In the former the groundwork for chaotic transport in the context of very large Reynolds number flows with rotation effects was laid, an ad hoc model based on experimental data was proposed, and surface of section studies showing qualitative agreement with experiments were made. In the latter a contour dynamics model was proposed and the linear theory of this model was treated. Here we consider a model based on the linear theory of a realistic model of the eastward jet. Surface of section studies are supplemented with analytical estimates.

In Sec. 2 a brief discussion of the SMS experiment is given along with the derivation of the underlying model equation that describes the quasigeostrophic flow in the experiment. Section 3 contains our proposed model for the stream function. Using linear stability analysis we find the values of the frequencies and mode numbers of the relevant Rossby waves. This analysis is then compared with the experiment. In Sec. 4 the stream function is used as a Hamiltonian for particle trajectories, and further comparisons with the experimental results are made. Poincaré sections obtained by numerical integration of Hamilton's equations are used to study the barriers to transport and the mixing properties of the system. Also the Chirikov overlap criterion (Chirikov 1979) is applied to produce an estimate for the onset of global transport. In Sec. 5 we summarize and, finally, we present ideas regarding the problem of self-consistency.

2. Description of the System

The SMS experiment consists of an annular tank with a flat top and conical bottom (see Fig. 1). The entire system rotates and the experiments are performed at constant angular

velocity Ω. The flow deviates from rigid rotation because of the action of the Coriolis force on water that is pumped radially through ports that are located in concentric rings on the bottom. When water is pumped radially inward a co-rotating or eastward jet is produced. A perturbation of this jet or "zonal flow" (we use these terms interchangeably) excites Rossby waves. The resultant flow composed of the jet plus these waves possesses strong and robust barriers to transport; i.e. dye injected on one side of the jet is observed to mix rapidly on the same side, but generally does not cross the jet (SMS 1989,1991).

To model the system we start from the Navier-Stokes equations for an inviscid incompressible fluid in the frame rotating with the tank

$$\frac{\partial \mathbf{V}}{\partial t} + (\mathbf{V} \cdot \nabla)\mathbf{V} = -\frac{1}{\rho}\nabla P + 2\mathbf{V} \times \mathbf{\Omega} \tag{2.1}$$

$$\nabla \cdot \mathbf{V} = 0 \ , \tag{2.2}$$

where we have redefined the pressure term so that it includes the centrifugal force.

The usual inviscid boundary condition is adopted; i.e. at the walls of the container

$$\mathbf{V} \cdot \mathbf{n} = 0 \ , \tag{2.3}$$

where $\mathbf{n}$ is the normal vector to the surface of the tank and $\mathbf{V}$ is the fluid velocity at that boundary. The cartesian components of the fluid velocity are chosen so that u and v are in the horizontal plane of the tank and w is the component in the direction of the rotation vector. The fluid is assumed two-dimensional in the sense that $u = u(x,y,t)$ and $v = (x,y,t)$, an hypothesis that is well supported by particle streak photographs.

Integration of Eq. (2.2) along the vertical direction z gives

$$w(x,y,z,t) = -\left(\frac{\partial u}{\partial x} + \frac{\partial v}{\partial y}\right) z + \hat{w}(x,y,t) \ , \tag{2.4}$$

where $\hat{w}$ is the integration constant. Defining the depth function

$$h = h_T - h_B$$

where $h_B(x,y)$ represents the bottom topography and h_T the flat lid of the tank, and applying the boundary condition of Eq. (2.3) to Eq. (2.4) gives

$$\frac{1}{h}\frac{dh}{dt} = -\left(\frac{\partial u}{\partial x} + \frac{\partial v}{\partial y}\right) . \tag{2.5}$$

Here d/dt is the advective derivative in the horizontal direction,

$$\frac{d}{dt} = \frac{\partial}{\partial t} + u\frac{\partial}{\partial x} + v\frac{\partial}{\partial y} .$$

Taking the curl of Eq. (2.1) yields

$$\frac{1}{2\Omega+\omega}\frac{d}{dt}(2\Omega+\omega) = -\left(\frac{\partial u}{\partial x} + \frac{\partial v}{\partial y}\right) , \tag{2.6}$$

where ω is the scalar vorticity. Defining the potential vorticity

$$q = \frac{2\Omega+\omega}{h} ,$$

and combining Eqs. (2.5) and (2.6) results in the following conservation law:

$$\frac{dq}{dt} = 0 . \tag{2.7}$$

In the quasigeostrophic approximation it is assumed that all the fields can be expanded in a power series of the small Rossby number

$$\epsilon = \frac{U}{2\Omega L} ,$$

where U and L are typical velocity and length scales, respectively. Zeroth order in ϵ yields geostrophic balance and therefore the Taylor-Proudman theorem holds; i.e.

$$(\Omega \cdot \nabla)\mathbf{V}_0 = 0 .$$

Hence using (2.2) we can write

$$u_0 = -\frac{\partial \psi}{\partial y} \qquad v_0 = \frac{\partial \psi}{\partial x} . \tag{2.8}$$

The bottom topography of the tank is linear

$$h = h_0 + sr$$

and the design parameters of the tank are chosen so that $sr/h_0 \approx \epsilon$. Therefore, to first order the potential vorticity is

$$q_1 = (\nabla^2\psi - \beta r)/h_0 \ , \tag{2.9}$$

where h_0 is a constant and the coefficient β is defined by

$$\beta = \frac{2\Omega s}{h_0} \ .$$

Also the dimensionless beta coefficient β^* is defined by

$$\beta^* = \left(\frac{L^2}{U}\right)\beta \ .$$

In the barotropic model of atmospheres the beta coefficient is given by $(2\Omega\cos\theta_0)/R$, where θ_0 is the latitude and R the planetary radius. Thus, in the experiment the gradient of the Coriolis force is mimicked by the gradient in the depth. In both cases the gradient as measured by β is responsible for the propagation of the Rossby waves.

Substituting Eqs. (2.8) and (2.9) into Eq. (2.7) we conclude that to first order in ϵ, potential vorticity conservation implies the quasigeostrophic equation

$$\frac{\partial}{\partial t}\nabla^2\psi + \left\{\psi, \nabla^2\psi - \beta r\right\} = 0 \ , \tag{2.10}$$

where the bracket is defined as follows:

$$\{f, g\} = \frac{\partial f}{\partial x}\frac{\partial g}{\partial y} - \frac{\partial f}{\partial y}\frac{\partial g}{\partial x} \ .$$

3. A Model for the Stream Function

In this section we develop a model for the stream function that is consistent with the experimental results, and which is motivated by linear analysis of the quasigeostrophic equation.

Experimental evidence suggests a stream function composed of an azimuthally symmetric zonal flow with the presence of one or more propagating waves. Thus we assume

$$\psi(r,\theta,t) = \psi_0(r) + \sum_k \psi_k(r,\theta,t) \ ,$$

where ψ_0 represents a time independent zonal flow and

$$\psi_k = \varepsilon_k \phi(r)\, e^{i(n_k\theta - \omega_k t)} \tag{3.1}$$

represents a perturbation to this flow in the form of a propagating wave.

For the equilibrium solution ψ_0 we follow the lead of SMS (1991), where it is shown that the data for the azimuthal average of the azimuthal component of the velocity is well fit by a sech^2 profile. Therefore

$$\psi_0(r) = UL \tanh\left(\frac{r-r_0}{L}\right) \ , \tag{3.2}$$

where r_0 is the radius at which the velocity reaches its maximum value U. Note that ψ_0 is a solution of the quasigeostrophic equation (2.10).

To model ψ_k, we are guided by linear stability analysis. Substituting Eq. (3.1) into the quasigeostrophic equation (2.10) we have, to first order in ϵ_k, the Rayleigh-Kuo linear eigenvalue equation for ϕ,

$$(U_0 - c)\left[\phi'' - \alpha^2\phi\right] + (\beta - U_0'')\phi = 0 \ , \tag{3.3}$$

where $U_0 = \partial\psi_0/\partial r$. Here we have used the slab approximation, in which the curvature effects are neglected, and we have defined

$$\lambda = \frac{2\pi r_0}{n} \qquad c = \frac{\omega r_0}{n} \qquad \alpha = \frac{n}{r_0} \ , \tag{3.4}$$

where the eigenvalue c is in general a complex number $c = c_r + ic_i$. The slab approximation is adopted since estimates show that for the modes of interest curvature corrections are small.

Because Eq. (3.3) is invariant under time reversal, for each asymptotically stable mode with $c_i < 0$, there corresponds an unstable mode with $c_i > 0$. Therefore the only stable

situation corresponds to neutral propagating waves with $c_i = 0$. Also, the fact that the zonal flow U_0 is symmetric implies that the eigenfunctions have definite parity, either symmetric (sinuous modes) or antisymmetric (varicose modes) with respect to r_0.

A detailed analysis of this eigenvalue problem was done by Lipps (1962) and Kuo (1973); the relevant results are summarized in the stability diagram presented in Fig. 2, which is a plot of the wave number versus β^*. Observe that for $\beta^* > 2/3$ the system is stable. This is consistent with Rayleigh-Kuo inflection point theorem, which states that $U_0'' - \beta < 0$ is a sufficient condition for stability. When this condition is applied to the sech^2 profile the threshold value of 2/3 emerges. The solid curve represents the neutral symmetric waves (sinuous modes) with $c_i = 0$ and with $c = c_r > 0$. These are marginally stable states that lie between the asymptotically stable and unstable states. For each value of $\beta^* < 2/3$ there are two neutral symmetric waves with eigenfunctions given by

$$\phi(r) = UL\,\mathrm{sech}^2\left(\frac{r - r_0}{L}\right) \tag{3.5}$$

$$\alpha_{1,2} = \frac{\sqrt{2}}{L}\sqrt{1 \pm \Delta}\,, \tag{3.6}$$

where

$$\Delta = \sqrt{1 - \frac{3}{2}\beta^*}\,. \tag{3.7}$$

The phase velocities of these waves are

$$c_{1,2} = \frac{U}{3}\left[1 \pm \Delta\right]\,, \tag{3.8}$$

where the upper and lower signs correspond to the upper and lower branches of the solid curve, respectively. Using Eqs. (3.4), (3.6), and (3.8), the frequencies and mode numbers of these neutral waves are given by

$$\omega_{1,2} = \frac{\sqrt{2}}{3}\frac{U}{L}\left[1 \pm \Delta\right]^{3/2} \qquad n_{1,2} = \frac{\sqrt{2}}{L}\, r_0 \sqrt{1 \pm \Delta}\,. \tag{3.9}$$

The dots in Fig. 2 represent points of maximum growth rate for the unstable modes with a given value of β^*. These were obtained using results from the eigenvalue analysis of Kuo (1973). The dashed curve represents the neutral antisymmetric waves (varicose modes). Again, these states define the boundary between asymptotically stable and unstable perturbations. The unstable varicose modes lie underneath the curve, the asymptotically stable modes lie above the curve, and the neutral modes exist where β^* is greater than 1/2.

According to the experimental results reported by SMS, the state of the jet is very close to the marginally stable state; that is, β^* is close to 2/3. Therefore from the stability diagram we expect to have a range of unstable symmetric modes, whereas the antisymmetric modes are neutrally stable. This range of unstable sinuous modes will contain wave numbers in the interval (α_2, α_1) and wave velocities in the interval (c_2, c_1). Defining the frequency range $\delta\omega$ and mode number range δn in the unstable range as

$$\delta\omega = \omega_1 - \omega_2 \qquad \delta n = n_1 - n_2$$

we obtain from Eqs. (3.9)

$$\delta\omega = \sqrt{2}\left(\frac{U}{L}\right)\Delta + \mathcal{O}(\Delta^3) \qquad \delta n = \sqrt{2}\left(\frac{r_0}{L}\right)\Delta + \mathcal{O}(\Delta^3)\,. \tag{3.10}$$

Of all the unstable modes in the range, only those with integral wave numbers can grow, because only these satisfy the wavelength quantization boundary condition. This fact provides a mode selection mechanism and allows us to predict the number of different modes that will become unstable for a given value of β^*. For example, if we have a two-mode state then δn must be greater than or equal to one. Using Eq. (3.10) we see that in general, for the existence of a k-mode state,

$$k - 1 \leq \frac{r_0}{L}\sqrt{2}\,\Delta\,, \tag{3.11}$$

where terms of order Δ^3 have been neglected because near-marginal stability β^* is close to 2/3 and therefore Δ is small.

Figure 3 is a plot of the normalized mode number $n^* = (L/r_0)n$ and frequency $\omega^* = (L/U)\omega$ as functions of β^* for the symmetric modes. This figure is useful since given the experimentally determined jet parameters L, U and r_0, one can obtain the allowed modes and their frequencies.

Usually the experiments indicate that a dominant mode is present. Figure 2 can be used to predict the wave number and frequency of this dominant mode. One expects that the dominant mode will be the one with the largest growth rate and hence the one closest to the curve represented by the dots. Generally speaking, modes with lower n and ω grow faster.

Figure 4 is a plot of the mode number n versus $1/L$. The dots represent the experimental measurements from SMS (1989). Lines (a) and (b) are n_1 and n_2 as determined by Eq. (3.9) for $\beta^* = 0.546$, which is 18% below the marginal value, and $r_0 = 28\,\text{cm}$. Observe that the unstable modes are located in the region between these two lines. Line (c) is the prediction made by SMS assuming $\beta^* = 2/3$. It is evident from the figure that the experimental values are closer to the n_2 line. This is consistent with the results presented in the stability diagram of Fig. 2, which indicates that modes with the largest growth rate have lower α and hence n values. Specifically, modes with the largest growth rates have n values that lie between lines (b) and (c).

Although this argument is highly encouraging, it must be kept in mind that these experimental results are in the regime of high Reynolds numbers where nonlinear effects are likely to be important. New experiments conducted at lower Reynolds numbers may provide a better test of the present model. The study of the time evolution of the unstable modes is a complicated problem where nonlinear saturation and mode interaction should be taken into account. These nonlinear effects, although interesting and important, will not be considered in the present work. Rather, we make the simplifying assumption that the saturated state of the unstable modes is close to the neutral solutions. Since β^* is near 2/3 this is a reasonable assumption because there is not a great deal of free energy available to drive the mode.

Therefore, we take as the model for the stream function, the superposition of the zonal flow (3.2) and two modes corresponding to the neutral symmetric solution (3.5); i.e.

$$\psi = UL \tanh\left(\frac{r-r_0}{L}\right) + UL\,\mathrm{sech}^2\left(\frac{r-r_0}{L}\right)\{\varepsilon_1 \cos(n_1\theta - \omega_1 t) + \varepsilon_2 \cos(n_2\theta - \omega_2 t + \delta)\}\ , \tag{3.12}$$

where n_i and ω_i are given by Eq. (3.9).

We do not expect that the above stream function will capture precisely the details of the fluid motion, particularly in the nonlinear regime. However, as stated in the introduction, we are more interested in characterizing transport and mixing by using Hamiltonian mechanics, than in the exact modelling of the velocity field. Since Hamiltonian models possess generic behavior, we do expect that Eq. (3.12) will capture the basic transport and mixing properties of the fluid. Ultimately what is important for Hamiltonian chaos studies is the global shape of ψ_0 and ϕ, and the range of the frequencies of the waves. As we shall see in the next section, results from application of the Chirikov criterion to Eq. (3.12) do not depend critically on the exact form of the functions ϕ and ψ_0.

4. The Stream Function as a Hamiltonian — Island Overlap

Writing Eqs. (1.2) in polar coordinates, then invoking the slab approximation results in the following Hamiltonian equations for the fluid particle trajectories:

$$\dot{r} = -\frac{\partial H}{\partial \theta} \qquad \dot{\theta} = \frac{\partial H}{\partial r} \qquad H = \frac{1}{r_0}\psi\ ,$$

where ψ is given by Eq. (3.12). Upon making a canonical transformation to remove the time dependence in the second cosine,

$$\theta' = \theta - \left(\frac{\omega_2}{n_2}\right)t \qquad\qquad r' = r\ ,$$

we obtain

$$H' = \frac{UL}{r_0}\tanh\left(\frac{r'-r_0}{L}\right) + \frac{UL}{r_0}\,\mathrm{sech}^2\left(\frac{r'-r_0}{L}\right)\left\{\varepsilon_1\cos(n_1\theta' - \tilde{\Omega}t) + \varepsilon_2\cos(n_2\theta')\right\} - \left(\frac{\omega_2}{n_2}\right)r' \,, \tag{4.1}$$

where $\tilde{\Omega} = (n_2\omega_1 - n_1\omega_2)/n_2$.

Physically this transformation corresponds to a change from the reference frame of the tank to a frame moving with the phase velocity of the second wave. Using Eq. (3.9) we can write $\tilde{\Omega}$ as a function of Δ

$$\tilde{\Omega} = \frac{2\sqrt{2}}{3}\left(\frac{U}{L}\right)\Delta\sqrt{1+\Delta}\,. \tag{4.2}$$

Figure 5(a) displays a contour plot of the experimental stream function at a fixed time as obtained from the particle streak photographs (after Behringer *et al.* (1991)). Figure 5(b) shows a plot of contours of constant H' at a fixed time with parameters $r_0 = 25\,\mathrm{cm}$, $L = 6.4\,\mathrm{cm}$, $\beta^* = 0.64$, $U = 12\,\mathrm{cm/sec}$, $\varepsilon_1 = 0.1$, $\varepsilon_2 = 0.3$, $n_1 = 6$, and $n_2 = 5$. Evidently, the phase space topology of the Hamiltonian characterized by the shape of the wavy pattern, and the island chains on both sides of the central zonal flow agree qualitatively with the experimental stream function.

As is well known, the presence of only a single mode results in an integrable system, and so chaotic advection is not possible. However, when both modes are present chaotic behavior appears in the phase space. The size and localizations of the chaotic regions can be determined in rough approximation by means of the Chirikov (1979) overlap criterion. We apply the criterion to the following general Hamiltonian with two modes:

$$H = H_0(r) + \sum_{i=1}^{2}\varepsilon_i\, f_i(r)\cos(n_i\theta - \omega_i t)\,. \tag{4.3}$$

Resonances occur at locations where the frequency of the perturbation matches the unperturbed frequency; i.e.

$$n_i\left(\frac{\partial H_0}{\partial r}\right)_{r_i^*} = \omega_i \tag{4.4}$$

In the rotating tank system resonances exist where the phase velocity of a mode matches the azimuthal velocity of the zonal flow. Near a resonance the unperturbed phase space is distorted giving rise to an island chain with a width dependent upon the size of the perturbation. When the two modes are present the resonances compete and chaos ensues. The Chirikov criterion provides an estimate for the destruction of invariant surfaces between the resonances. According to the Chirikov criterion the last invariant surface between two such resonances is destroyed when the sum of the half widths of the two island separatrices formed by the resonances, but calculated independently of one another, equals the distance between the resonances; that is when

$$\frac{W_1}{2} + \frac{W_2}{2} = \left| r_2^* - r_1^* \right| \tag{4.5}$$

where W_i are the widths of the island separatrices, and r_i^* are the positions of the resonances.

To compute W_i we consider the Hamiltonian with only the ith-mode present

$$H_i = H_0(r) + \varepsilon_i \, f_i(r) \cos(n_i\theta - \omega_i t) \; ,$$

which in the frame moving with the phase velocity of mode becomes

$$H_i' = H_0(r') + \varepsilon_i \, f_i(r') \cos(n_i\theta') - \left(\frac{\omega_i}{n_i}\right) r' \; . \tag{4.6}$$

Expanding about the resonance by letting $r' = r_i^* + p$ and assuming small p and ε_i yields

$$H_i'(\theta', p) = \frac{p^2}{2m_i} + k_i \cos(n_i\theta') \; ,$$

where

$$m_i = \left(\frac{\partial^2 H_0}{\partial r^2} \right)^{-1}_{r_i^*} \qquad k_i = \varepsilon_i \, f_i(r^*) \; . \tag{4.7}$$

In this "pendulum approximation," the width of the island is given simply by the distance between the pendulum separatrices

$$W_i = 4\sqrt{k_i |m_i|} \; . \tag{4.8}$$

Thus, using this approximation, the overlap condition becomes

$$\sqrt{k_1|m_1|} + 2\sqrt{k_2|m_2|} = |r_2^* - r_1^*| \,. \tag{4.9}$$

For the rotating experiments of interest ($\partial H_0/\partial r$) is the velocity profile of the zonal flow, therefore generically it is a convex and nearly symmetric function with respect to r_0. Hence, Eq. (4.4) will in general have two solutions, in contrast to the usual case in Hamiltonian mechanics, where the frequency is a monotonic function of the action and only one resonance line is created by each mode. (We mention in passing that the Hamiltonian map that describes this system violates the so-called twist condition.) The situation is shown schematically in Fig. 6, where $r^*_{1,2+}$ and $r^*_{1,2-}$, the locations of the resonance pairs, are equidistant from the center of the zonal flow located at r_0.

Since each mode creates two resonances, two types of overlap are possible. One type occurs when the resonance located at r^*_{2+} overlaps that located at r^*_{1+}, while both remain above r_0, and because of symmetry r^*_{2-} and r^*_{1-} will simultaneously overlap below r_0. This first type results in symmetric bands of chaos separated by a band of nearly integrable behavior spanning the maximum of the zonal flow. Thus we refer to this case as *banded chaos*. Since the phase space is two dimensional, the invariant tori of the nearly integrable region near r_0 divide the phase space into two regions precluding global transport. The second type of chaos, referred to as *global chaos*, occurs when the resonances conspire to destroy the invariant barriers dividing the two sides of the zonal flow. One would expect this to occur when the resonance at r^*_{2+} overlaps that at r^*_{1-}. This is a degenerate situation since resonance r^*_{2+} must "pass through" resonance r^*_{1+}, which undoubtedly destroys the validity of the isolated resonance picture. Many additional significant subresonances will appear. Nevertheless, for this situation one requires that the locations of these resonances (r^*_{2+} and r^*_{1-}) get sufficiently close to r_0 to interact and so we (questionably) apply Chirikov's criteria to this case, in an attempt to describe global chaos.

To illustrate these general ideas let us apply them to our linear model. Substituting

$$H_0 = \frac{UL}{r_0}\tanh\left(\frac{r-r_0}{L}\right) \qquad f_i(r) = \frac{UL}{r_0}\,\mathrm{sech}^2\left(\frac{r-r_0}{L}\right) \quad i=1,2 \tag{4.10}$$

into (4.9) we get the overlap criterion

$$C_\pm(\beta^*,\varepsilon_1,\varepsilon_2) = \frac{\sqrt{2\varepsilon_1}}{(1-\gamma_1)^{1/4}} + \frac{\sqrt{2\varepsilon_2}}{(1-\gamma_2)^{1/4}} - \Big|\,|\mathrm{sech}^{-1}(\sqrt{\gamma_1})| \pm |\mathrm{sech}^{-1}(\sqrt{\gamma_2})|\,\Big| = 0\ , \tag{4.11}$$

where the lower and upper signs correspond to banded and global chaos, respectively, and we have defined

$$\gamma_{1,2} \equiv \frac{c_{1,2}}{U} = \frac{1}{3}[1 \pm \Delta]\ . \tag{4.12}$$

Figure 7(a) is a plot in the $\varepsilon_1, \varepsilon_2$ plane of the curves $C_- = 0$ for values of β^* 10%, 20%, 30%, 40%, and 50% below the 2/3 marginal value. For a given value of β^* the region above the corresponding curve represents the values of ε_1 and ε_2 where overlap occurs, whereas the region below this curve represents non-overlapping values. Observe that banded chaos is a very typical situation occurring for almost all values of ε_i and for β^* close to 2/3.

The values of $\varepsilon_1(\varepsilon_2)$ for which a given curve touches the $\varepsilon_1(\varepsilon_2)$ axis represent the situation where the resonance line of the second (first) mode touches the separatrix of the resonance created by the first (second) mode. In this situation it is clear that we will have overlap for arbitrarily small values of $\varepsilon_2(\varepsilon_1)$. Figure 8 depicts Poincaré sections showing the onset of this banded chaos. The sections were computed with fourth-order Runge-Kutta numerical integration of the Hamiltonian (4.1) with $U = 12\,\mathrm{cm/sec}$, $r_0 = 25\,\mathrm{cm}$, $L = 6.4\,\mathrm{cm}$, $n_1 = 6$, $n_2 = 5$, $\omega_1 = 1.133$, $\omega_2 = 0.656$, $\beta^* = 0.64$, $\varepsilon_2 = 0.3$, and (a) $\varepsilon_1 = 0.03$, and (b) $\varepsilon_1 = 0.1$. Observe that banded chaos appears even for the small value of $\varepsilon_2 = 0.03$ as predicted by the Chirikov criterion. The width of the chaotic bands on both sides of the jet increases with the value of ε_1 but the invariant tori near the radius r_0 remain. These results are consistent with the experiments, where bands of chaotic advection are usually seen on both sides of the wavy jet, but the jet is resilient and acts as a barrier to transport between the inner and outer parts of the tank.

The onset of global chaos is of obvious importance for transport, and is determined by the destruction of the wavy jet barrier, i.e., the last invariant torus. Figure 7(b) is the locus of points defined by $C_+ = 0$. Regions above these curves represent values of $\varepsilon_1, \varepsilon_2$ for which (in the pendulum approximation) the resonance at r^*_{1+} overlaps that at r^*_{2-}. From the plot we note that this regime is very unlikely to appear for small values of epsilon. Observe that if $r^*_{1\pm}$ and $r^*_{2\pm}$ were located very near r_0, then small values of ε_1 and ε_2 could achieve overlap. However, this condition is physically difficult to meet since the phase velocities of the sinuous Rossby waves are bounded above by $2U/3$, and thus within the confines of linear theory the closest a resonance can be to r_0 is given by $r^*_c = L\,\mathrm{sech}^{-1}\sqrt{2/3}$. Also, the quantization condition separates the resonances; e.g., the second resonance is limited by Eq. (3.11) to have $r^*_{2+} \geq L\,\mathrm{sech}^{-1}\sqrt{\left(1 - \frac{L}{\sqrt{2}\,r_0}\right)/3}$, which translates into a distance further from r_0 than r^*_c. These restrictions on the locations of the resonances explain why the curves of Fig. 7(b) are in regions of large ε_i. Clearly, the robustness of the wavy jet barrier observed in the experiment is consistent with linear theory.

If we ignore the restriction that the ε_i's be small, as required for the validity of the pendulum approximation and linear theory, then in practice we have found that the overlap condition of $C_+ = 0$ provides a useful means for choosing parameters. If we are beneath the $C_+ = 0$ curve then global chaos does not occur. In this case the isolated resonance picture is a good one and we expect the zonal flow invariant surfaces. However, if we are above the curve the breakdown of the above approximation and the isolated resonance picture make conclusions suspect. In practice we have observed bounding invariant surfaces for very large ε_1 and ε_2. Alternatively, if one ignores the restriction imposed on the phase velocities by linear theory, then application of $C_+ = 0$ for resonances placed ad hoc near r_0 with small ε_i's, is consistent with numerical results we have obtained that show global chaos. In particular a trajectory with the parameters of Fig. 8(b), but with $\omega_1 = 1.728$, $\omega_2 = 1.200$, $\varepsilon_1 = \varepsilon_2 = 0.3$, and initial conditions $r(t = 0)$ 21 cm, $\theta(t = 0) = \pi$ wanders freely. Since the system is

forced by the radial pumping, it is possible that the frequencies of some of the excited modes could be shifted from linear theory. Such results are interesting, but greater confidence awaits the measurement of the frequencies, and most likely, a nonlinear calculation is required.

5. Summary and Discussion

A main objective of this paper was to study chaotic advective transport in quasigeostrophic flows. Of particular interest was to compare theory with the SMS rotating tank experiments. In Sec. 1 we reviewed notions pertaining to chaotic advective transport, while in Sec. 2 we presented a derivation of the quasigeostrophic equation that models the SMS experiment. Section 3 was devoted to obtaining a model for the stream function, composed of a zonal flow equilibrium with linear eigenfunctions, which was seen to be consistent with experimental results and linear theory. The theoretical contour plots are in qualitative agreement with the experimental stream function contour plots (Fig. 5), and linear theory was shown to correctly predict the onset of observed sinuous Rossby waves with the appropriate mode numbers (Fig. 4). The model stream function was used in Sec. 4 to study chaotic transport. Here the Chirikov overlap criterion was applied to the model, and it was observed that banded chaos, i.e., regions of chaos bounded by invariant surfaces (in particular those of the zonal flow barrier), is to be expected. This is in agreement with the experiment. Also, it was shown that global chaos, and hence transport across the zonal flow, is inconsistent with linear theory and in general requires resonances with phase velocities near the peak velocity of the zonal flow equilibrium. This appears to explain the lack of global chaos in the experiments.

In conclusion we make some qualitative comments on self-consistency; i.e. consistency between the existence of chaos in the fluid element trajectories and conservation, or near conservation, of potential vorticity. As noted in Secs. 1 and 4, chaos requires a time dependence in the stream function that cannot be removed by a frame change. If finite degree-of-freedom

Hamiltonian system serve as a guide for the more complicated infinite degree-of-freedom Hamiltonian system of (2.10), one expects periodic solutions in the vicinity of equilibrium states. Such a solution would be a time periodic stream function, and corresponding potential vorticity function, that exactly solves (2.10). But, in infinite dimensions the situation is significantly more complex and this naive analogy is not sufficient. In fact, paradoxically, one can argue that chaos and conservation of q (constancy along trajectories), are inconsistent.

Consider a time periodic stream function (Hamiltonian) $\psi(\mathbf{r}, t)$ such as that of Eq. (4.1). Generically, hidden invariants do not exist and one expects the trajectories as given by Eqs. (1.2) to exhibit chaos. Since these trajectories are uniquely given by their initial values we write

$$\mathbf{r} = \mathbf{r}(\mathbf{r}_0, t) \tag{5.1}$$

where $\mathbf{r}_0 = (x_0, y_0)$ denotes the position at time $t = 0$. Since Eq. (2.10) is equivalent to the statement that potential vorticity is constant along the trajectories, we can write its solution in the form

$$q(\mathbf{r}, t) = q_0(\mathbf{r}_0(\mathbf{r}, t)) \tag{5.2}$$

where $\mathbf{r}_0(\mathbf{r}, t)$ is obtained from (5.1) by running the orbit backwards in time and $q(\mathbf{r}, 0) = q_0(\mathbf{r})$. Generally, sensitivity to initial conditions is taken as a working definition of chaos. Hence, as time proceeds we expect $\mathbf{r}(\mathbf{r}_0, t)$ to depend sensitively on $\mathbf{r}_0$ and evidently $\mathbf{r}_0(\mathbf{r}, t)$ will depend sensitively on $\mathbf{r}$. Therefore in general q will depend sensitively on $\mathbf{r}$. But, $\psi(\mathbf{r}, t)$ is not sensitively dependent on $\mathbf{r}$ and therefore the same follows for $q = \nabla^2\psi - \beta r$. Thus we arrive at an apparent contradiction between chaos and conservation of potential vorticity.

The contradiction can be resolved without destroying potential vorticity conservation, simply by requiring that q_0 and hence q be constant, or nearly constant, in regions where the trajectories are highly chaotic. The sensitivity of $\mathbf{r}_0$ on $\mathbf{r}$ is thus smeared out in q; the q-contours are widely separated and do not reveal the underlying Lagrangian chaos. This

picture is verified in a qualitative manner by plotting q-contours. Generally, we observe for our linear model that banded chaos occurs in regions where q tends to be flat. This is an indication of self-consistency in the model. Note that local constancy of q does not preclude time dependence in ψ, only that the time dependence occurs in a function that is spatially harmonic; i.e. $\nabla^2\psi = 0$.

In reality potential vorticity is not exactly conserved; as chaotic motion begins to produce highly irregular potential vorticity contours, one expects because of sharp gradients that viscous dissipation will redistribute potential vorticity on small scales. However, on larger (course grained) scales the motion can behave in a nondissipative manner and questions of self-consistency are relevant. Experimentally it is difficult to resolve scales much below a millimeter. Verification of these ideas awaits further experimental and theoretical efforts.

Acknowledgments

The authors would like to acknowledge many helpful conversations with W. Holloway, S. Meyers, T. Solomon, and H. Swinney,. Also the authors acknowledge the support of the U.S. Department of Energy contract #DE-FG05-80ET-53088. PJM would like to acknowledge the hospitality of the Aspen Center for Physics, where a portion of this work was carried out. DdCN acknowledges support by the Instituto de Ciencias Nucleares, Universidad Nacional Autonoma de Mexico.

References

H. Aref, J. Fluid Mech. **143**, 1 (1984).

R.P. Behringer, S.D. Meyers and H.L. Swinney, Phys. Fluids A **3** (May) (1991).

B.V. Chirikov, Phys. Reports **52**, 263 (1979).

W. Horton, Plasma Physics and Controlled Fusion **27**, 937 (1985).

W. Horton, Phys. Reports **192**, 1, (1990).

H.L. Kuo, Adv. Applied Mech. **13**, 247 (1973).

F.B. Lipps, J. Fluid Mech. **12**, 397 (1962).

J.M. Ottino, Ann. Rev. Fluid Mech. **22**, 207 (1990).

J. Pedlosky, *Geophysical Fluid Dynamics,* Second Ed. (Springer-Verlag, New York, 1987).

L.M. Polvani and J. Touma, to appear in *Nonlinear Phenomena in Atmospheric and Oceanic Sciences,* G. Carnevale and R. Pierrehumbert eds., (Springer-Verlag, New York, 1991).

J. Sommeria, S.D. Meyers, and H.L. Swinney, Nature **337**, 58 (1989).

J. Sommeria, S.D. Meyers, and H.L. Swinney, in *Nonlinear Topics in Ocean Physics,* ed. A. Osborne (North Holland, Amsterdam, 1991).

Figure Captions

1. Depiction of the rotating annulus experiment of SMS (1989, 1991). The inner radius $r_1 = 10.8\,\text{cm}$ and the outer radius $r_2 = 43.2\,\text{cm}$; the depth of the tank increases from $h_1 = 17.1\,\text{cm}$ at the inner radius to $h_T = 20.3\,\text{cm}$ at the outer radius, resulting in a conical bottom topography with a slope -0.1. The whole system rotates at a constant angular velocity Ω in the range from 0 to 25 rad/sec. The action of the Coriolis force on fluid pumped radially at the bottom of the tank generates an eastward (corotating) jet.

2. Stability diagram for the sech^2 velocity profile. The solid curve represents neutral symmetric (sinuous) modes, while the dashed curve represents neutral antisymmetric (varicose) modes, both with $c > 0$. These curves define boundaries between asymptotically stable and unstable states. (The wording on the figure refers to the sinuous modes of interest.) For β^* close to 2/3 there is a band of sinuous modes that grow whereas the varicose modes are neutral for $\beta^* > 1/2$. The dots represents the unstable sinuous modes with maximum growth rate for a given value of β^*.

3. Normalized mode number $n^* = (L/r_0)n$ and frequency $\omega^* = (L/U)\omega$ as a function of β^*.

4. Mode number n as a function of $1/L$. Lines (a) and (b) are n_1 and n_2 as functions of $1/L$ for β^* 18% below the marginal value. Line (c) is the prediction made by SMS assuming $\beta^* = 2/3$. The dots are the experimental values obtained by SMS. Linear theory predicts that the dots should lie between lines (c) and (a).

5. a) Contour plot of streamlines deduced from particle streak photograph of the flow [after Behringer *et al.* (1991)]. b) Phase space topology for Hamiltonian (4.1) at a fixed time with parameters: $U = 12\,\text{cm/sec}$, $r_0 = 25\,\text{cm}$, $L = 6.4$ $n_1 = 6$, $n_2 = 5$,

$\omega_1 = 1.133$ rad/sec, $\omega_2 = 0.656$ rad/sec, $\beta^* = 0.64$, $\varepsilon_1 = 0.1$ and $\varepsilon_2 = 0.3$.

6. Depiction of isolated resonance pairs used in the overlap criterion. Banded chaos occurs when the resonance at r^*_{1+} overlaps that at r_{2+}, and simultaneously because of symmetry r^*_{1-} and r^*_{2-} overlap. An estimate for global chaos is given by the overlap of r^*_{2+} with r^*_{1-}.

7. a) Banded chaos as determined by plot of $C_-(\varepsilon_1, \varepsilon_2, \beta^*) = 0$ [Eq. (4.11)] for values of β^* equal to 10%, 20%, 30%, 40%, and 50% below the marginal value of 2/3. For a given β^* the region above the corresponding curve represents the values of ε_1 and ε_2 for which the Chirikov criterion predicts banded chaos. The region below the curve represents non-overlapping values of ε_1 and ε_2. b) Global chaos as determined by plot of $C_+(\varepsilon_1, \varepsilon_2, \beta^*) = 0$ [Eq. (4.11)] for values of β^* equal to 10%, 20%, 30%, 40%, and 50% below the marginal value of 2/3. For a given β^* the region above the corresponding curve represents the values of ε_1 and ε_2 for which the Chirikov criterion predicts global chaos. The region below the curve represents non-overlapping values of ε_1 and ε_2.

8. Poincaré sections obtained by Runge-Kutta fourth order numerical integration of Hamiltonian (4.1) with parameters: $U = 12\,\text{cm/sec}$, $r_0 = 25\,\text{cm}$, $L = 6.4\,\text{cm}$, $n_1 = 6$, $n_2 = 5$, $\omega_1 = 1.133$ rad/sec, $\omega_2 = 0.656$ rad/sec, $\beta^* = 0.64$, $\varepsilon_2 = 0.3$ and increasing values of ε_1: (a) $\varepsilon_1 = 0.03$ and (b) $\varepsilon_1 = 0.1$. To generate the sections we consider the evolution of two groups of ten particles equally spaced between the inner and outer radius of the tank. One group located at $\theta = 0$ and the other at $\theta = 2\pi/10$.

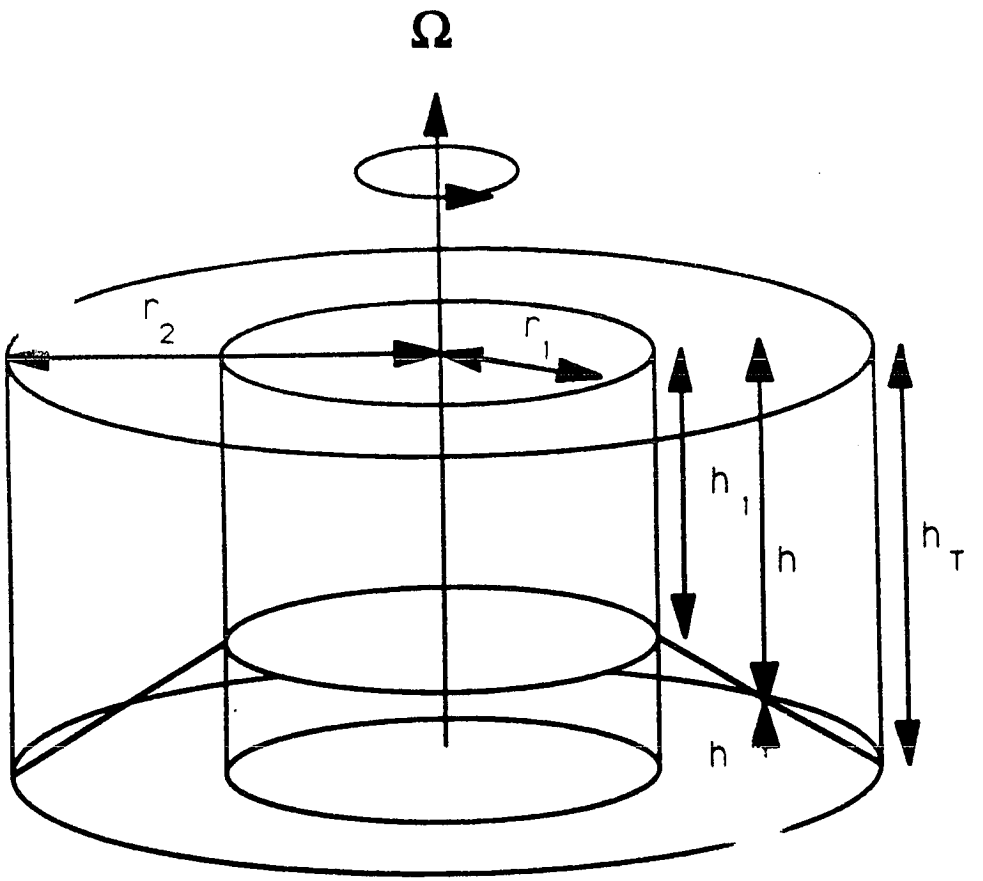

Fig. 1

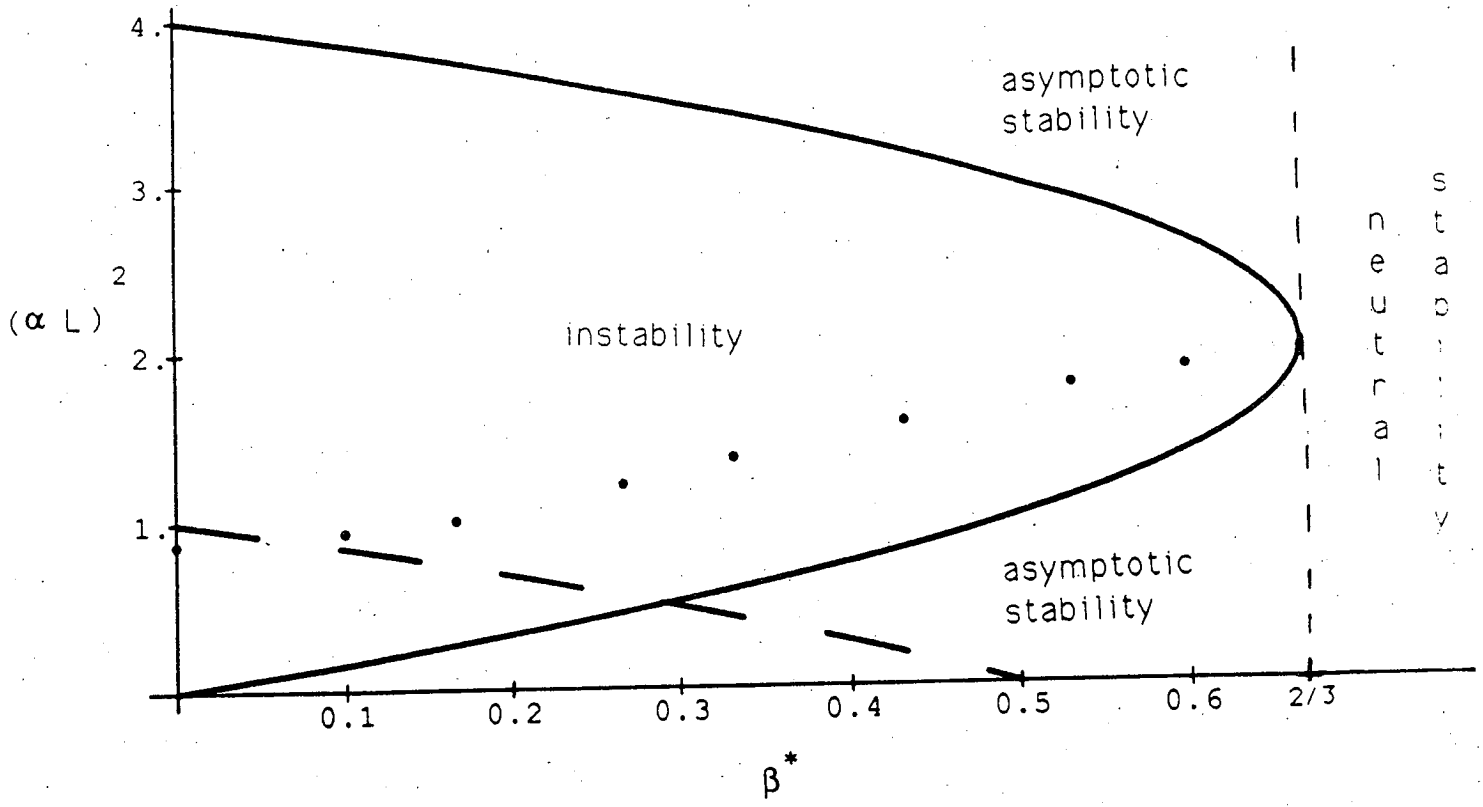
4.
3.
2.
1.
(α L)
2
asymptotic
stability
instability
asymptotic
stability
neutral
stability
0.1
0.2
0.3
0.4
0.5
0.6
2/3
β*

Fig. 2

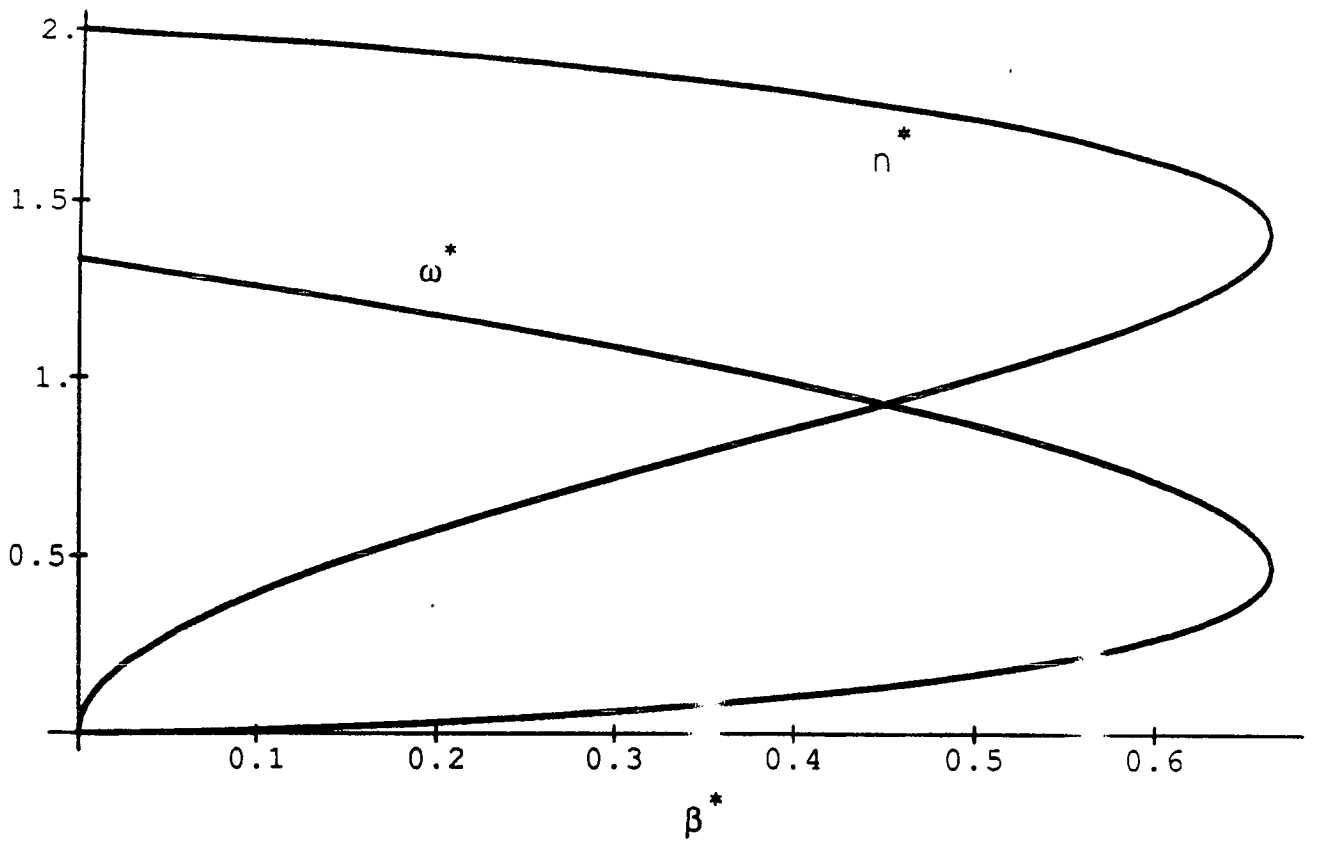

Fig. 3

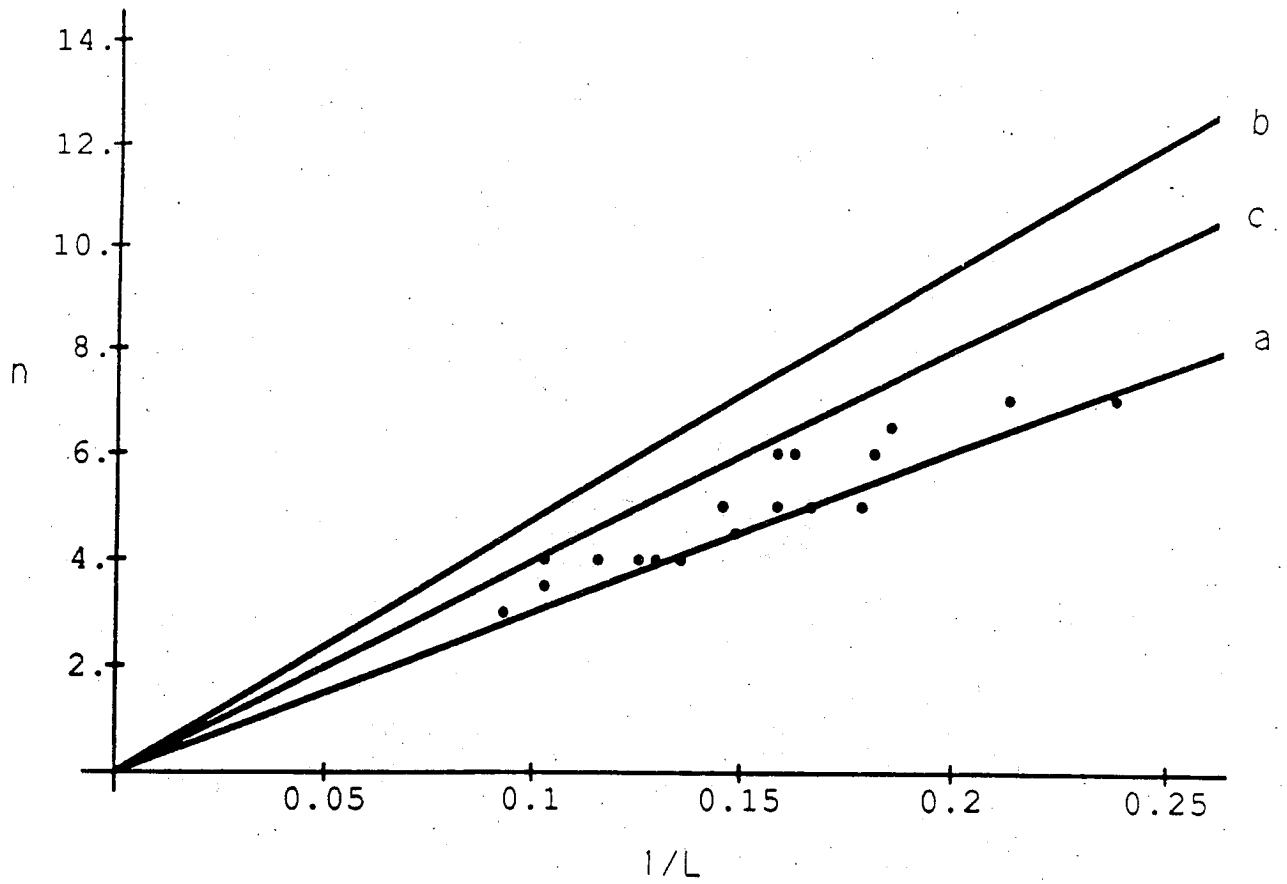

Fig. 4

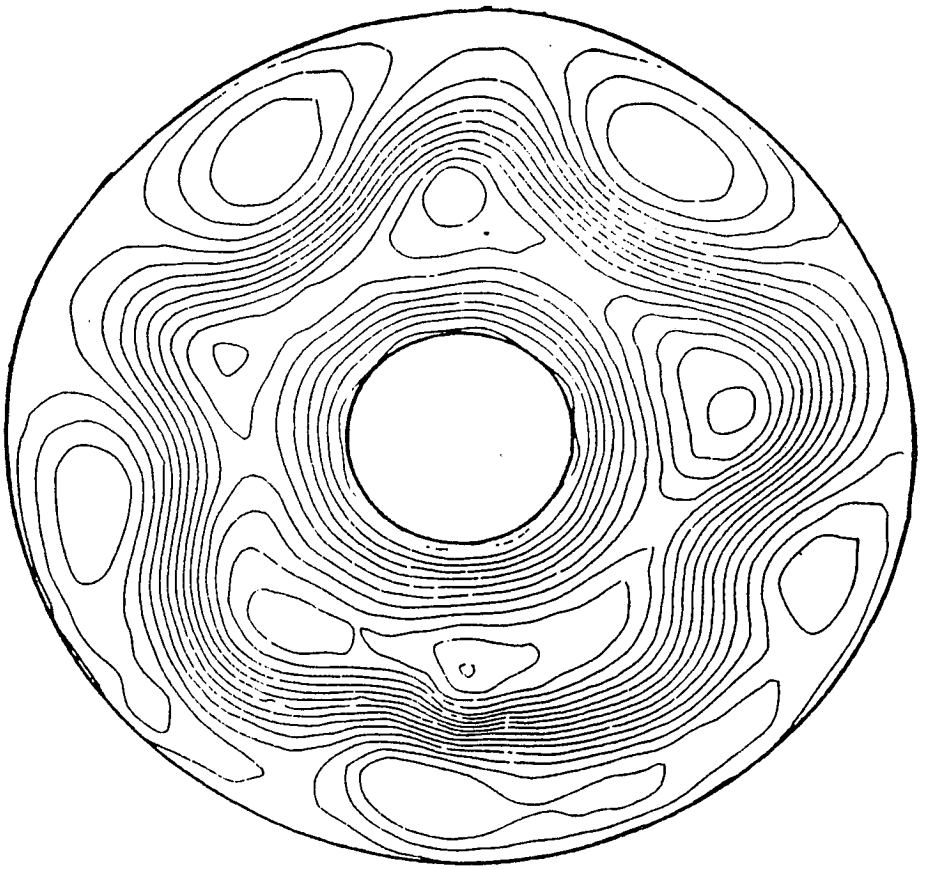

Fig. 5(a)

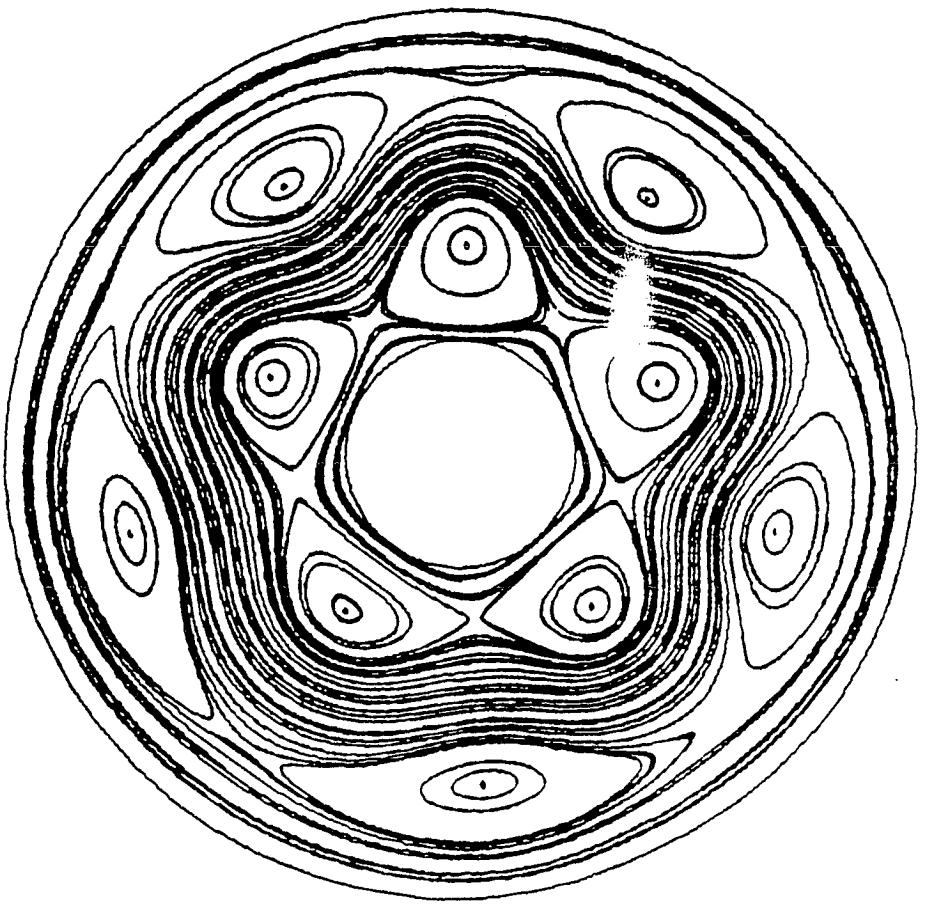

Fig. 5(b)

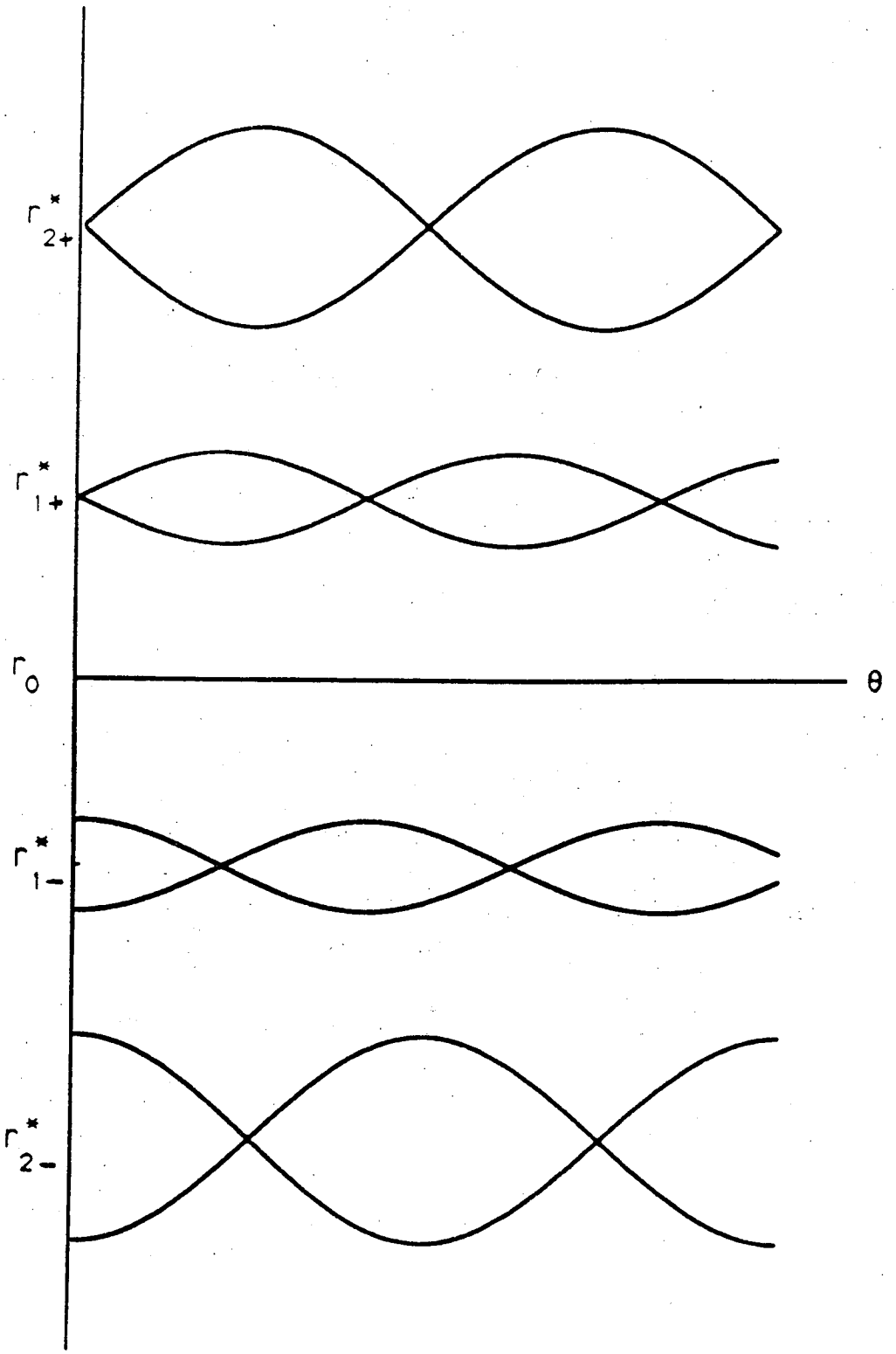

Fig. 6

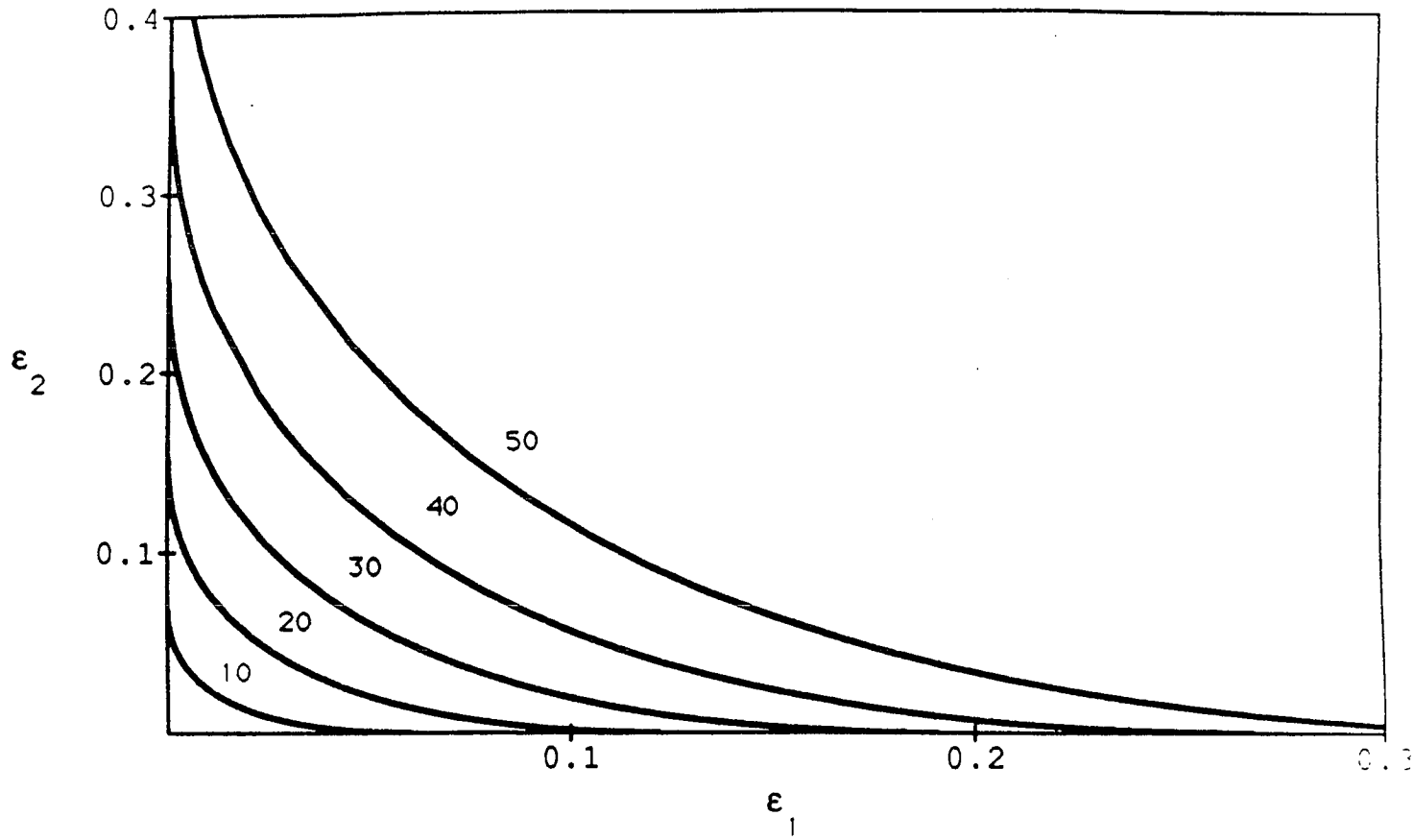

Fig. 7(a)

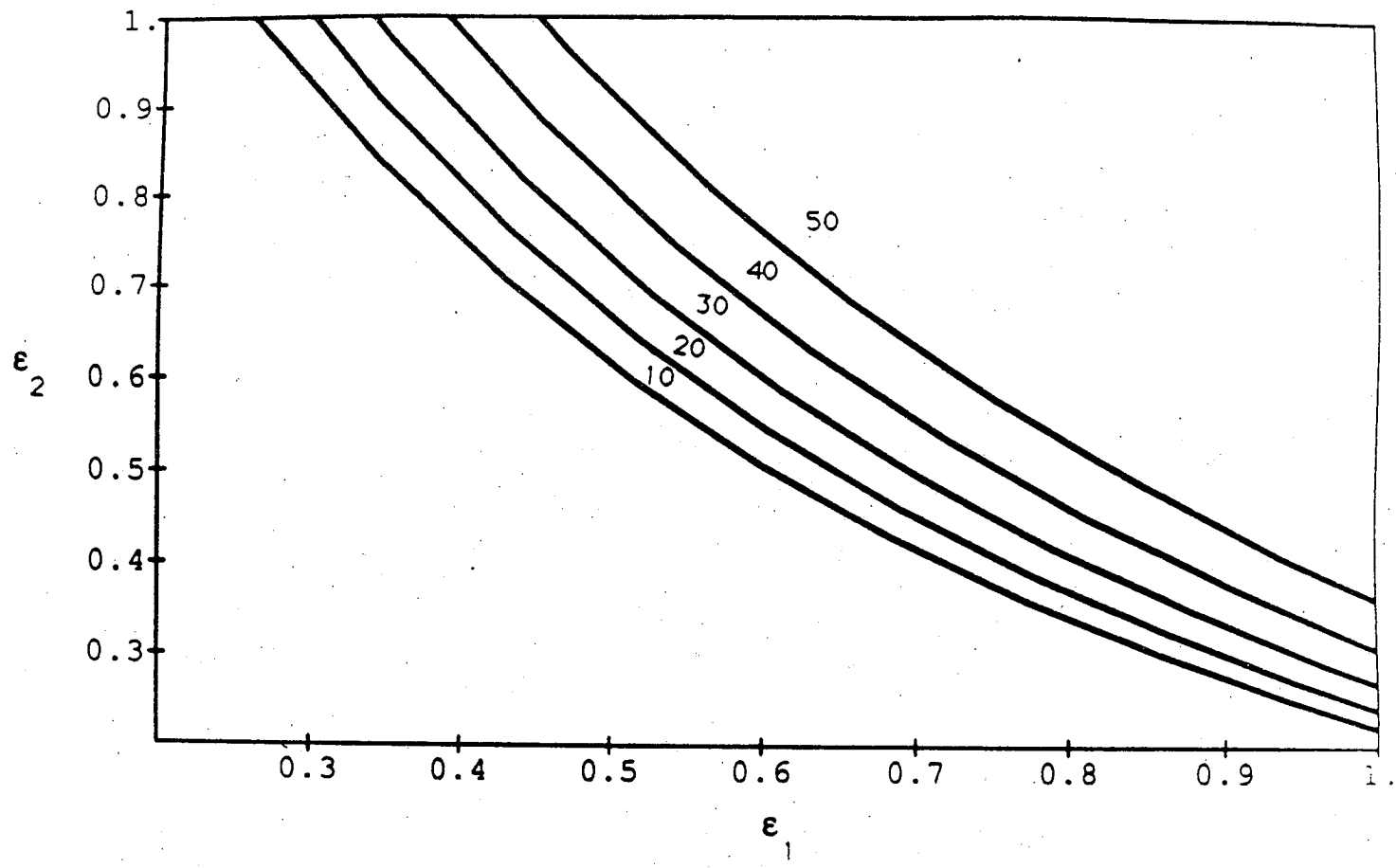
1.
0.9
0.8
0.7
0.6
0.5
0.4
0.3
ε_2
50
40
30
20
10
0.3
0.4
0.5
0.6
0.7
0.8
0.9
1.
ε_1

Fig. 7(b)

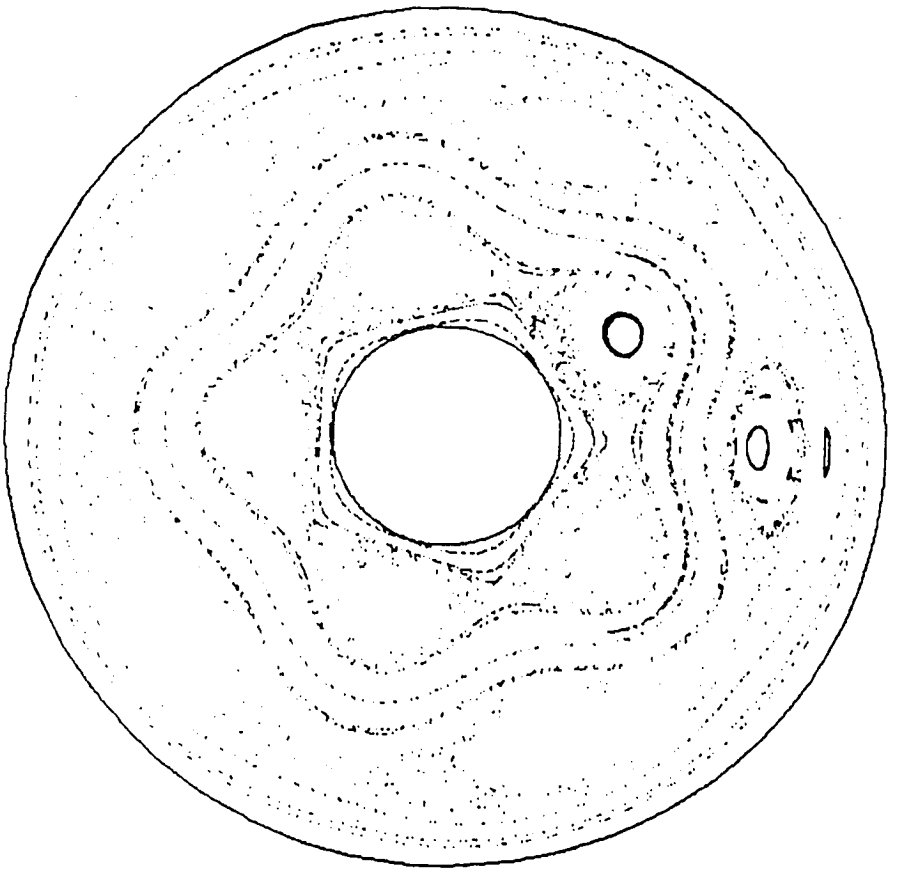

Fig. 8(a)

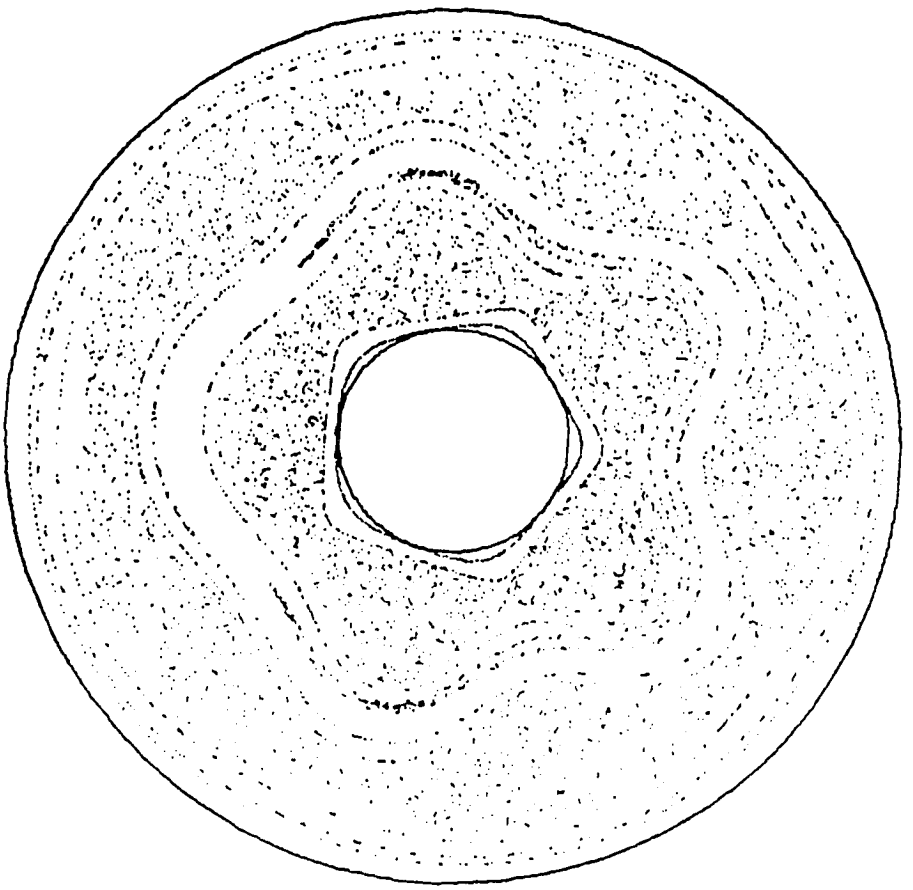

Fig. 8(b)